





Collinear Rashba-Edelstein effect in nonmagnetic chiral materials

Karma Tenzin ^{1,2}, Arunesh Roy,¹ Frank T. Cerasoli,³ Anooja Jayaraj ⁴, Marco Buongiorno Nardelli ^{4,5}
and Jagoda Stawińska ¹

¹Zernike Institute for Advanced Materials, University of Groningen, Nijenborgh 4, 9747AG Groningen, Netherlands

²Department of Physical Science, Sherubtse College, Royal University of Bhutan, 42007 Kanglung, Trashigang, Bhutan

³Department of Chemistry, University of California, Davis, California 95616, USA

⁴Department of Physics, University of North Texas, Denton, Texas 76203, USA

⁵The Santa Fe Institute, Santa Fe, New Mexico 87501, USA



(Received 28 March 2023; revised 27 October 2023; accepted 15 November 2023; published 11 December 2023)

Efficient generation and manipulation of spin signals in a given material without invoking external magnetism remain one of the challenges in spintronics. The spin Hall effect (SHE) and Rashba-Edelstein effect (REE) are well-known mechanisms to electrically generate spin accumulation in materials with strong spin-orbit coupling (SOC), but the exact role of the strength and type of SOC, especially in crystals with low symmetry, has yet to be explained. In this study, we investigate REE in three different families of nonmagnetic chiral materials, elemental semiconductors (Te and Se), metal silicides (FeSi and OsSi), and semimetal disilicides (TaSi₂ and NbSi₂), using an approach based on density functional theory. By analyzing spin textures across the full Brillouin zones and comparing them with REE magnitudes calculated as a function of chemical potential, we link specific features in the electronic structure with the efficiency of the induced spin accumulation. Our findings show that magnitudes of REE can be increased by (i) the presence of one particular type of spin-orbit field, for example, Weyl-type SOC that yields a radial spin texture, (ii) high spin polarization of bands along one specific crystallographic direction, and (iii) low band velocities. By comparing materials possessing the same crystal structures but different strengths of SOC, we conclude that larger SOC may indirectly contribute to the enhancement of REE. It yields greater spin splitting of bands along specific crystallographic directions, which prevents canceling the contributions from the oppositely spin-polarized bands over wider energy regions and helps maintain larger REE magnitudes. Surprisingly, however, for some materials, the velocity of electronic states plays an even more important role in regulating the REE magnitudes than SOC. Additionally, these magnitudes are strongly influenced by changes in band topology. We believe that our results will be useful for designing spintronics devices and may aid further computational studies searching for efficient REE in materials with different symmetries and SOC strengths.

DOI: [10.1103/PhysRevB.108.245203](https://doi.org/10.1103/PhysRevB.108.245203)

I. INTRODUCTION

Many properties of crystals are driven by their structure and symmetries, which not only allows for explaining existing phenomena but also facilitates predicting yet unexplored effects or functionalities in families of materials that are structurally identical. One of the most intriguing symmetries in nature is chirality, which describes objects that cannot be mapped onto their mirror images by rotations and translations, just like human hands [1]. Chiral molecules and crystals typically have two energetically equivalent configurations called enantiomers that are mirror reflections of each other. They may respond differently to external fields, which gives rise to a variety of intriguing properties and phenomena, for example, unconventional superconductivity [2], Kramers-Weyl fermions [3], magnetic structures (skyrmions) [4,5], and chirality-dependent spin transport that manifests as chirality-induced spin selectivity (CISS) in organic molecules [6–8] and the collinear Rashba-Edelstein effect (REE) in chiral materials [9–11]. The observation of these effects ignited vigorous debates on fundamental factors that determine them quantitatively, such as the interplay of chirality and

spin-orbit coupling (SOC), whose exact role remains to be explored.

In our previous studies, we performed first-principles calculations for chiral Te and used the semiclassical Boltzmann transport theory to estimate the spin accumulation generated via REE. We showed that the current-induced spin accumulation is chirality dependent and parallel to the applied charge current [11,12], which is in line with recent experimental studies reporting gate-tunable charge-to-spin conversion in Te nanowires [10]. Similar effects were also investigated in chiral dichalcogenides and metal disilicides, in which itinerant electrons become spin polarized over macroscopic distances in response to the electric field [13–15]. Even though some of these works suggest that the observed spin accumulation is the manifestation of CISS, in analogy to the spin signals measured in chiral molecules, the connection between the collinear REE in solid-state materials and CISS in molecular systems has not yet been established. Understanding the key ingredients that contribute to these effects is therefore vital.

Here, we report a computational study of three families of chiral compounds, elemental semiconductors Te and Se, metal silicides FeSi and OsSi, and metal disilicides TaSi₂

and NbSi₂, to compare the current-induced spin accumulation in materials with the same crystallographic structure but different strengths of SOC. By analyzing crystal symmetries and electronic structures, we identify three main factors that may enhance the current-induced spin accumulation in chiral materials: (i) the presence of one particular type of spin-orbit field (SOF), for example, a Weyl-type spin texture that gives rise to the parallel spin momentum locking, (ii) nondegenerate bands that are spin polarized entirely along a specific crystallographic direction, and (iii) low band velocities. At the same time, stronger SOC broadens energy regions with a large REE rather than increasing its magnitude. Additionally, we find that spin accumulation is strongly influenced by band topology. This paper is organized as follows: in Sec. II, we describe density functional theory (DFT) calculations and give a summary of the REE implementation in the framework of Boltzmann transport theory. In Sec. III, we provide an extended analysis of the electronic structure and spin transport in Te and Se. Section IV details a similar extended analysis for FeSi and OsSi. Section V describes the analogous properties of the metal disilicides TaSi₂ and NbSi₂, and Sec. VI summarizes the paper.

II. COMPUTATIONAL DETAILS

Our *ab initio* calculations were performed using the QUANTUM ESPRESSO simulation package [16,17]. We used the fully relativistic pseudopotentials to treat the ion-electron interaction [18], and the Perdew, Burke, and Ernzerhof (PBE) version of the generalized gradient approximation functional for each material except for Se, for which we employed PBE for solids (PBEsol) [19,20]. Elemental semiconductors and semimetallic disilicides structures were constructed using hexagonal unit cells containing three and nine atoms, respectively. Metal silicides were modeled using cubic unit cells containing eight atoms. We adopted the experimental lattice constants $a = 4.80$ (4.78) Å and $c = 6.59$ (6.57) Å for NbSi₂ (TaSi₂) reported in previous studies [15,21] and relaxed their atomic positions using energy and force convergence criteria set to 10^{-5} Ry and 10^{-4} Ry/bohr, respectively. For the remaining structures, volume relaxations were performed, resulting in lattice constants of $a = 4.52$ (4.50) Å and $c = 5.81$ (5.05) Å for Te (Se) and $a = b = c = 4.45$ (4.79) Å for FeSi (OsSi). Brillouin zone (BZ) integrations were performed on k grids of $16 \times 16 \times 12$ for metal disilicides; $22 \times 22 \times 16$ and $16 \times 16 \times 14$ for Te and Se, respectively; and $20 \times 20 \times 20$ for metal silicides. For the orbital occupation scheme, we chose Gaussian smearing of 0.002 Ry (NbSi₂/TaSi₂, FeSi/OsSi), 0.001 Ry (Te), and 0.05 Ry (Se). The electronic structures of the elemental semiconductors were corrected by adding the Hubbard parameters calculated via the Agapito-Curtarolo Buongiorno Nardelli (ACBN0) approach [22]. The values of U were estimated to 3.81 and 3.56 eV for Te and Se, respectively. SOC was included self-consistently in all the calculations, except for the relaxations.

The isoenergy surfaces, spin textures, and spin accumulation were evaluated using the open-source PYTHON package PAOFLOW, which projects the wave functions from the *ab initio* self-consistent calculations onto the pseudo-atomic orbitals (PAO) to construct tight-binding (TB) Hamiltonians

[23,24]. These Hamiltonians represent an exact mapping of the DFT solution on a finite atomic orbital basis and thus have the same accuracy as the original first-principles calculations [25,26]. The PAO Hamiltonians were further interpolated to much denser k grids of $80 \times 80 \times 60$ for NbSi₂/TaSi₂, $200 \times 200 \times 180$ for Te, $200 \times 200 \times 200$ for Se, and $300 \times 300 \times 300$ for FeSi/OsSi to converge the final REE calculations [27]. The current-induced spin accumulation was calculated in the framework of semiclassical Boltzmann transport theory as implemented in our previous works [11,12]. In this approach, the net spin density generated by the applied charge current j^A is expressed as

$$\delta s^j = \chi^{ji} j_i^A, \quad (1)$$

where j and i are the directions of induced magnetization and applied charge current, respectively, and χ^{ji} is a response tensor which we call the current-induced spin polarization (CISP) tensor, spin accumulation tensor, or Edelstein susceptibility interchangeably throughout this work. Assuming constant relaxation time and a diagonal form of the charge conductivity tensor [28–30], χ^{ji} can be expressed as

$$\chi^{ji} = -\frac{\sum_{\mathbf{k}} \langle \mathcal{S} \rangle_{\mathbf{k}}^j v_{\mathbf{k}}^i \frac{\partial f_{\mathbf{k}}}{\partial E_{\mathbf{k}}}}{e \sum_{\mathbf{k}} (v_{\mathbf{k}}^i)^2 \frac{\partial f_{\mathbf{k}}}{\partial E_{\mathbf{k}}}}, \quad (2)$$

where \mathbf{k} stands for k vectors in reciprocal space, $\langle \mathcal{S} \rangle$ denotes the expectation value of the spin operator, v is the Fermi velocity vector, f is the nonequilibrium distribution function, E is the energy, and e is the elementary charge. The summations are performed over all bands for any given energy. All these quantities can be computed using the TB Hamiltonians; additionally, we used a Gaussian function to approximate the derivative of the Fermi-Dirac distribution as discussed in Ref. [27]; all calculations were performed at $T = 0$ using the adaptive smearing approach. The tensor elements χ^{ji} were evaluated automatically in PAOFLOW, and the allowed components of the tensor were determined via the symmetry analysis [11,12,31].

It is worth mentioning that our choice of definition of the response tensor χ^{ji} , which involves a charge current instead of an electric field, facilitates a comparison of the calculated magnitudes with measured spin accumulation per unit volume in response to a specific electric current. For example, in Ref. [9] the results for Te were estimated from the nuclear magnetic resonance measurements, and a net spin density induced by the current of 100 A/cm² was reported.

III. ELEMENTAL TELLURIUM AND SELENIUM

Geometry and electronic structures. Elemental Te and Se share the trigonal crystallographic structure described by space groups (SGs) $P3_121$ (152) and $P3_221$ (154) for the right- and left-handed enantiomers, respectively. The atoms are arranged along the spiral chains running along the c axis that stem from each corner of the a - b plane; they interact with each other via weak van der Waals forces [see Fig. 1(a)]. Both enantiomers possess three rotational symmetries C_2 whose axes are located within the a - b plane, whereas the right-handed and left-handed structures can be distinguished by

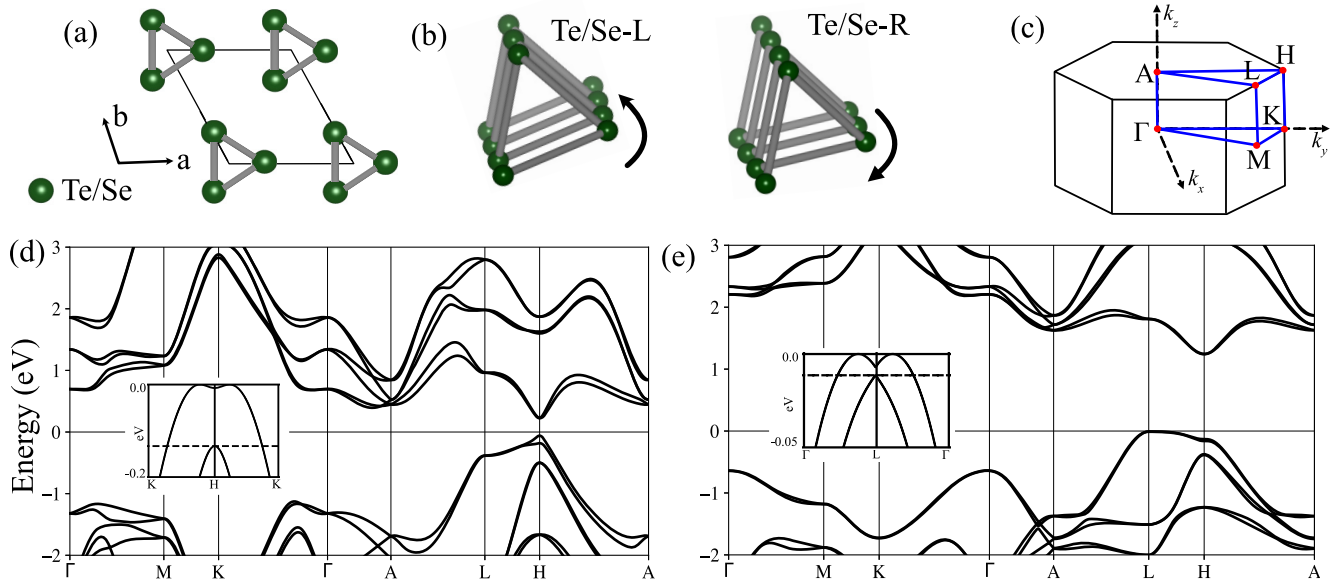


FIG. 1. (a) Top view of the crystal structure of trigonal Te/Se. (b) Zoom of three Te/Se atoms at one of the corners of the unit cell sketched for the left-handed and right-handed Te/Se. The chirality is determined by the threefold screw symmetry along the c axis. (c) High-symmetry lines of the Brillouin zone (BZ). Electronic structures of (d) Te and (e) Se along the high-symmetry lines shown in (c). Valence band maxima (VBMs) for Te and Se are along the K - H and Γ - L lines, respectively; zoomed-in views of bands around the VBM are shown in the insets, and the band edges are marked by the dashed lines. Fermi levels are set at the VBM.

the threefold screw symmetries 3_1 and 3_2 along the c axis [Fig. 1(b)].

The calculated band structures, illustrated in Figs. 1(d) and 1(e), indicate that elemental Te and Se are semiconductors with band gaps of 0.28 and 1.25 eV, respectively. The electronic structure of Te is in good agreement with previous studies [9–11,32–34], including the value of the band gap, which is quite close to the measured one (330 meV) [35]. The experimental band gap of Se (~ 1.9 eV) [36–38] is more difficult to reproduce via standard DFT+ U calculations [32]. However, as both semiconductors are intrinsically p type doped [39–41], only the valence bands will contribute to the charge and spin transport, and our electronic structures are sufficiently accurate to evaluate REE. The typical values of doping in Te lie within the range of 10^{14} – 10^{17} holes/cm³ [39,40], which, based on our calculations, corresponds to energies up to 30 meV below the valence band maximum (VBM). Similarly for Se, the measured hole concentrations are reported to be approximately 10^{14} /cm³ [42].

The electronic structures of Te and Se exhibit distinct characteristics around the Fermi level. In Te, the VBM resides in proximity to the H point (K - H line), while in Se, it is located near the L point (Γ - L line). This difference arises from the diverse arrangements of p orbitals comprising the valence states [32]. The bands reveal strong influence of SOC, manifesting mostly as spin splitting of bands. These features are more apparent in Te; for example, the splitting of the topmost valence band at the H point is 108 meV, which is much higher than in Se (~ 4.3 meV at the L point). We found that the band just below the topmost valence band emerges at 117 (12) meV below the VBM for Te (Se), as shown in the inset in Fig. 1(d) [Fig. 1(e)]. While the exact splitting depends

on the k vector, the difference between the materials can be partly explained by the strength of spin-orbit interaction (SOI) (around 2.7 times larger for the p orbitals of Te compared with those of Se atoms) [43,44].

Isoenergy surfaces and spin textures. Figure 2 shows the isoenergy surfaces and spin textures (STs) calculated a few tens of meV below the Fermi level E_F , which corresponds to the slight p -type doping observed in experiments [39–41]. The isoenergy surface of Te [Fig. 2(a)] consists of dumbbell-shaped hole pockets that appear at each corner of the BZ [11]. However, at energies closer to the Fermi level, the valence band consists of a pair of pockets located around H . These pockets undergo a Lifshitz transition, merging into a single pocket similar to the one shown in Fig. 2(a) at around 9 meV below the VBM. Figure 2(b) displays the (quasi-two-dimensional) isoenergy surface of Se at 8.0 meV below the VBM. This band undergoes the Lifshitz transition at 7.7 meV below the VBM. Because the electronic and spin transport will be determined mostly by these pockets, we further analyze the symmetry of SOF around the H (L) point of Te (Se).

Using the Bilbao Crystallographic Server (BCS) [45,46], we found that the H point of SGs $P3_121$ and $P3_221$ is described by the D_3 wave-vector point group symmetry, which can host only the Weyl-type SOC [47]. The projection of SOF plotted in Fig. 2(c) indeed indicates a radial ST pattern around the H point, although we notice that it is mostly polarized along the k_z direction [11,12]. Similarly, we found that the L point of Se is described by the D_2 point group symmetry, which allows for the combination of Weyl and Dresselhaus SOFs [47]. The projection of STs onto the plane of the pocket [Fig. 2(e)] shows a radial spin orientation which in some regions deviates toward a quasi-persistent pattern, similar to

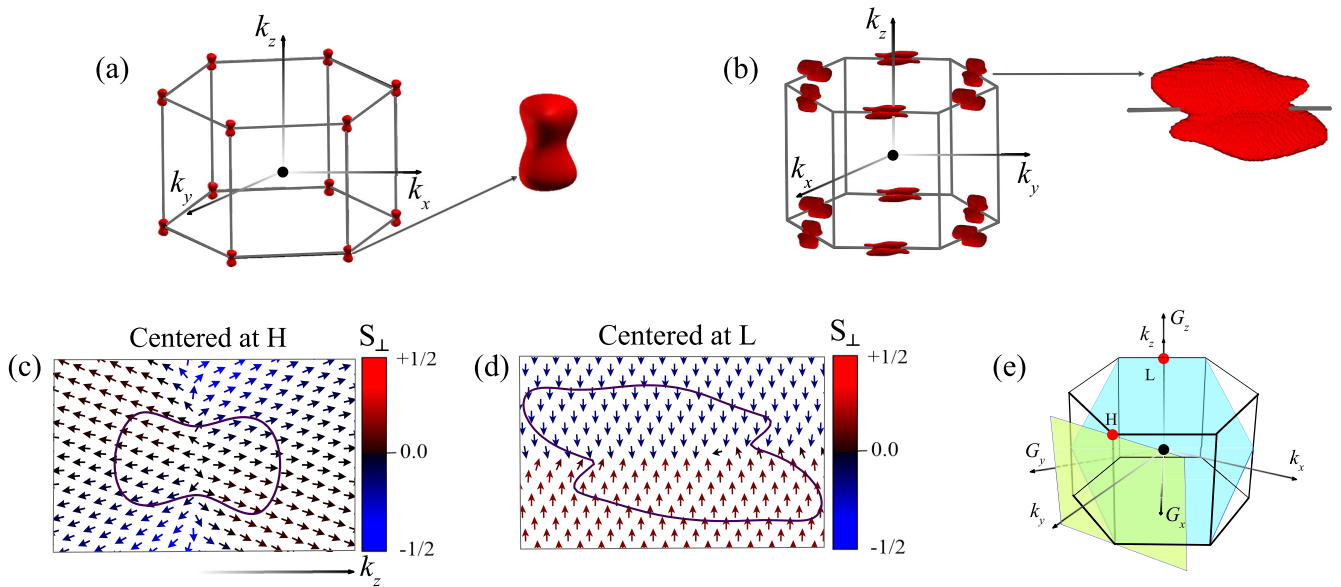


FIG. 2. (a) Isoenergy surface of Te at energy $E = -30$ meV. The zoom shows details of the dumbbell-shaped hole pockets that reside at each H point of the BZ. (b) The isoenergy surface of Se at energy $E = -8$ meV. All these pockets are centered at the L points. (c) The spin texture of the hole pocket shown in (a) projected onto the equivalent (110) plane centered at the H point. The plane is shown as a yellow frame in (e). (d) The spin texture of the isoenergy surface of Se shown in (b) projected onto the plane of the (quasi-two-dimensional) pocket and centered at the L point. The plane (0,100,169) is shown as a turquoise frame in (e). The color bars represent spin texture components perpendicular to the planes; all spin projections are normalized to $\pm\hbar/2$. (e) Schematic view of the planes used for the projections shown in (c) and (d).

the case for Te. These persistent spin textures (PSTs) are quite different from the typical hedgehoglike vector fields typically associated with radial spin textures. However, they are compatible with D_3 symmetries, which allow for anisotropic coefficients in the expansion terms of the spin texture [48]. Importantly, PSTs may reduce spin scattering and lead to an increase in spin lifetimes, protecting spin accumulation over large distances [11,49,50].

Spin accumulation. We performed the symmetry analysis using BCS and found that the REE tensor possesses only diagonal components $\chi^{xx} = \chi^{yy} \neq \chi^{zz}$ [12]. Their magnitudes plotted as a function of the chemical potential are displayed in Figs. 3(a) and 3(b) for the left-handed Te and Se, respectively. Since the electronic structures of left- and right-handed enantiomers differ only by the sign of the ST, the REE magnitudes are opposite, thereby yielding a chirality-dependent spin accumulation. The REE estimated for Te is the highest along the z axis, with the largest value of $8.0 \times 10^{10} \frac{\hbar}{\text{Acm}}$ occurring slightly below the Lifshitz transition energy. The spin accumulation along the x and y directions is significantly lower, albeit within the same order of magnitude, with a maximum of $2.5 \times 10^{10} \frac{\hbar}{\text{Acm}}$ at 90 meV below the VBM. In the case of Se, the weaker SOC implies overall lower magnitudes of the REE, but the behavior of $\chi(E)$ differs from that of Te, indicating that the exact electronic structure plays a relevant role. For example, the maximal value of χ^{zz} ($-4.2 \times 10^{10} \frac{\hbar}{\text{Acm}}$) around the Lifshitz transition energy is negative. Moreover, in contrast to Te, χ^{xx} changes sign close to E_F , which indicates that it can be switched via electrostatic gating. Overall, our results showing a sharp drop in the induced spin densities close to the Lifshitz transition energy are consistent with previous theoretical work on the REE [51].

To gain more insight into the peculiar $\chi(E)$ plots, we analyze both spin polarization and the velocity of states around and below the VBMs. To this aim, we show spin- and velocity-resolved isoenergy contours in Figs. 4 and 5 calculated for Te and Se, respectively. The most pronounced feature that can be noticed in these contours is that the spins are polarized predominantly along the z direction for Te, while the polarization is more evenly distributed along all three directions for Se. Conversely, velocity contours indicate that the Fermi velocity vectors are equally polarized in all three directions for both materials. Although the velocities play a role in the modulation of the spin accumulation curves, we deduce from these contour plots that the nature of the spin texture is the key feature that determines spin accumulation in this case. For Te, χ^{zz} increases gradually for energy above the band edge position of the second band up to a level slightly above the Lifshitz transition energy. The χ^{xx}/χ^{yy} components remain constant for the majority of the energy spectrum above the band edge position of the second band. A sudden drop in all tensor components below ~ -117 meV can be attributed to the emergence of the second/inner band with an opposite spin texture. Spin accumulation plots of Se follow the same trends, except that the peaks are sharper and narrower owing to much lower band splitting; that is, the second/inner band with opposite spin texture for Se emerges at around 12 meV below the VBM. Below this value, the spin accumulation decreases sharply due to the compensating effect.

Overall, the analysis of Te and Se allows us to draw a few important conclusions. While the purely radial spin texture leads to larger magnitudes of the REE compared to materials with bands endowed with mixed ST patterns [12], the exact features of $\chi(E)$ curves are sensitive to the direction

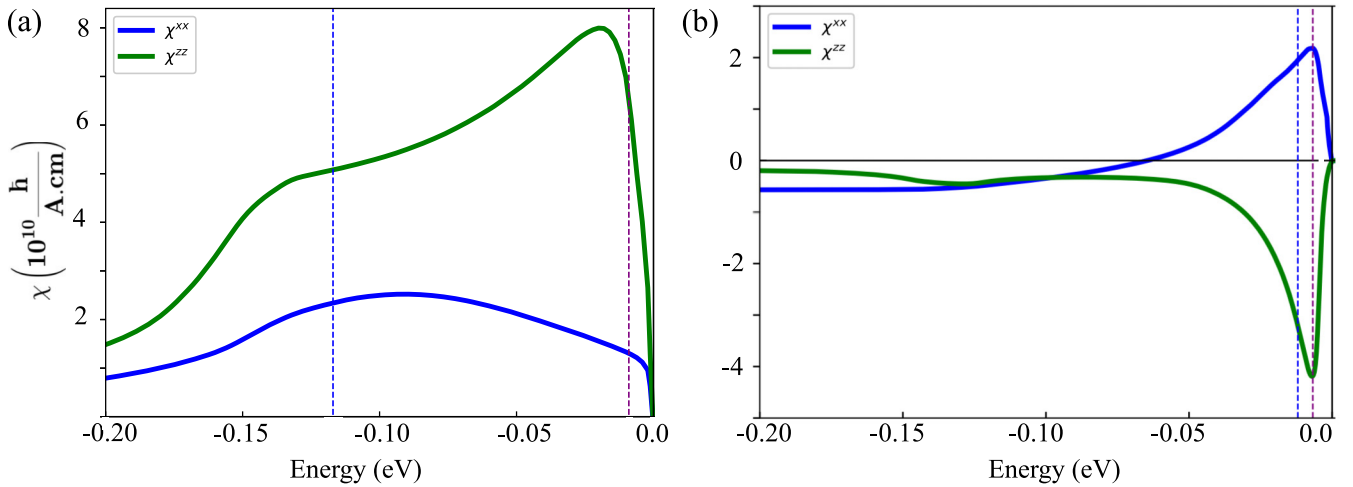


FIG. 3. (a) Current-induced spin accumulation vs chemical potential calculated for the left-handed Te. Green and blue lines represent the χ^{zz} and χ^{xx} components of the REE tensor. The element χ^{yy} is omitted as it is identical to χ^{xx} [12]. (b) The same as in (a), but calculated for Se. The blue dashed line corresponds to the edges of the second valence bands at -117 (-12) meV for Te (Se). The purple dashed line represents the position of the Lifshitz transition of the topmost valence band at -9 (-7.7) meV for Te (Se). $\chi(E)$ of the right-handed enantiomers (not shown) are exactly opposite by symmetry.

of spin polarization, band velocities, and Lifshitz transition energies. The existence of a band where the average spin polarization is along a specific direction leads to the enhancement of the spin accumulation along that direction. We also note that stronger SOC yields greater splittings between oppositely spin-polarized bands, as in the case of Te, so the

regions with larger χ cover wider energy ranges. The impact of velocity components on spin accumulation is less evident in these materials, as our analysis is limited to the energy range where $\chi(E)$ exhibits its peak. These energy ranges predominantly encompass a single band with similar velocity features across most contours. The velocity becomes

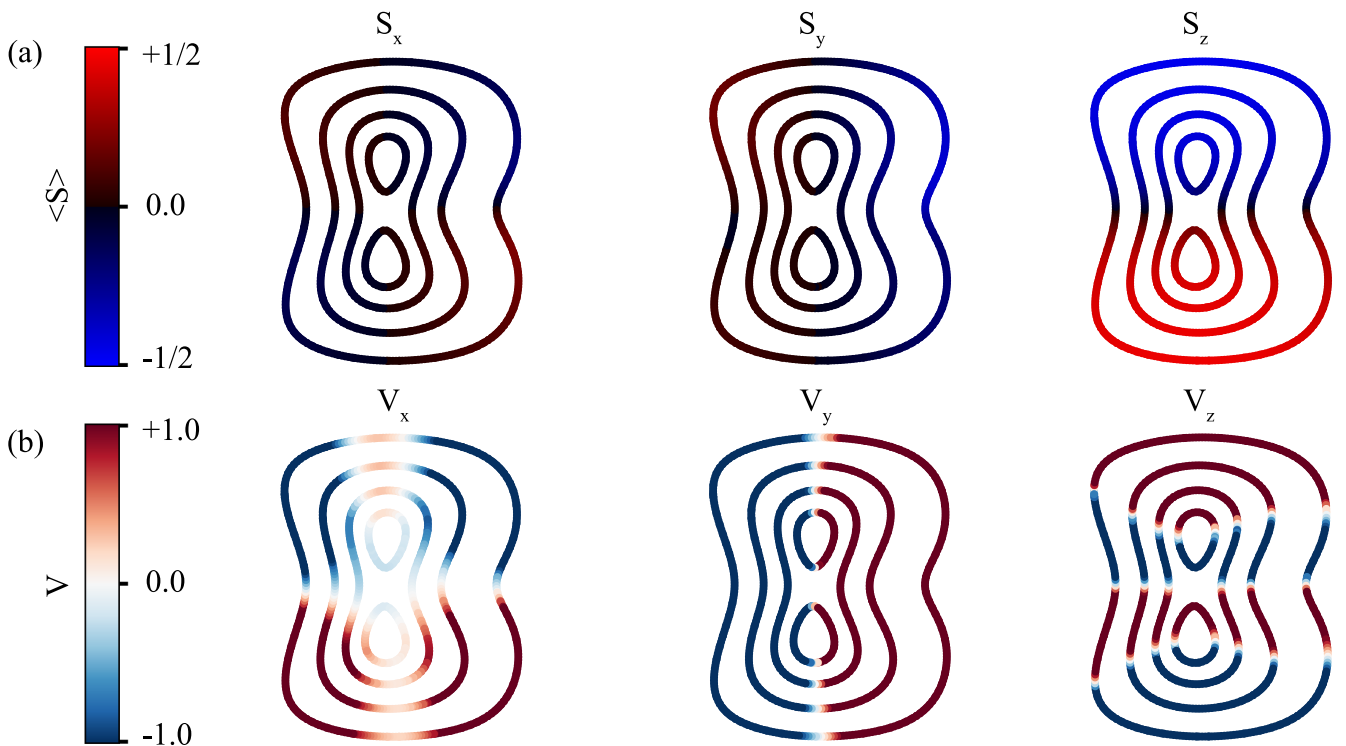


FIG. 4. (a) Different components of the spin texture of Te calculated on the rectangular face of the BZ displayed in Fig. 13(c) and centered around the H point. The contours correspond to isoenergy levels of -8 , -23 , -53 , and -103 meV below the VBM. (b) The same, but for velocity projections. Velocity plots are normalized to ± 1.0 corresponding to maximum/minimum values of $\pm 7.75 \frac{eV \text{ bohr}}{\hbar}$. Spins are normalized to $\pm \hbar/2$. All the considered isoenergies belong to the same band.

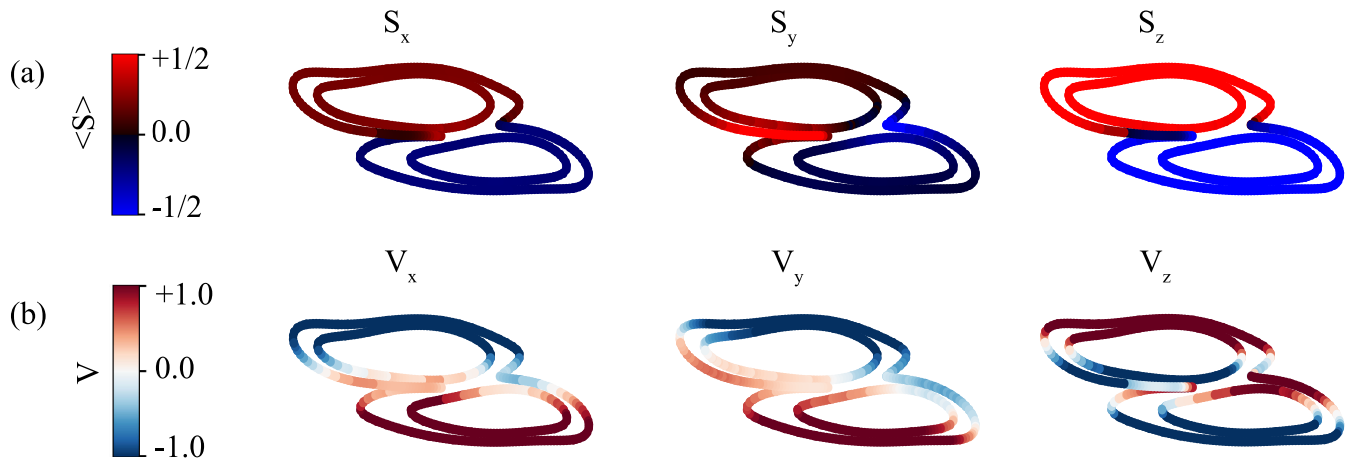


FIG. 5. (a) Different components of the spin texture of Se calculated on the plane shown in Fig. 2(e) and centered around the L point. The contours correspond to isoenergy levels of -5 and -8 meV. (b) The same, but for velocity projections. Velocity plots are normalized to ± 1.0 corresponding to maximum/minimum values of $\pm 3.79 \frac{eV \text{ bohr}}{\hbar}$. Spins are normalized to $\pm \hbar/2$. Both isoenergies belong to the same band.

more important in materials in which spin accumulation peaks are influenced by multiple bands with distinct velocities. In the next sections, we will study spin accumulation in chiral materials with more sophisticated band structures and spin textures to reveal other properties that can enhance spin accumulation.

IV. METAL SILICIDES

Geometry and electronic structures. We will now focus on two structurally identical metal (M) silicides, FeSi and OsSi, belonging to a well-known crystal system called B20; it has received increased attention in recent years owing to the large topological charges and Fermi arcs that can emerge at the surface [52–55]. The symmetries of these materials are described by space group $P2_13$ (198), which is achiral but contains only operations of the first kind, thus allowing chiral structures [56]. The right-handed and left-handed crystals are described by the same space group, and for the purpose of this work, RL structure is defined with M - M and Si-Si chains exhibiting right- and left-handedness, respectively, while LR structure is defined with M - M and Si-Si chains exhibiting left- and right-handedness; the corresponding crystal structures are shown in Fig. 6. The electronic structure calculations performed for FeSi and OsSi indicate that both are semiconductors with band gaps of 120 and 180 meV, respectively (see

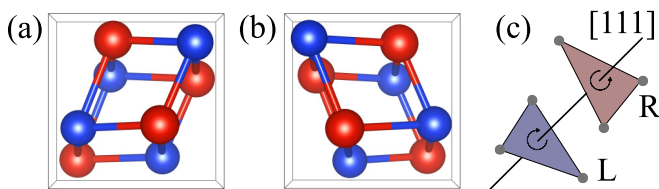


FIG. 6. Crystal structure of metal silicides; red (blue) spheres represent M (Si) ions. The RL configuration shown in (a) depicts M (Si) ions with right- (left-) handedness, while the LR configuration in (b) depicts M (Si) ions with left- (right-) handedness along the $[111]$ direction. An illustration of handedness for this class of material is shown in (c).

Fig. 7). The estimated spin splitting of the FeSi valence band is about 40 meV (at the X point), while the splitting for OsSi is found to be around 330 meV (along the Γ - X path). Our band structures are in good agreement with previous studies [56–58].

Isoenergy surfaces and spin textures. Close to the Fermi level, the two topmost valence bands of both materials give rise to isoenergy surfaces in the form of small pockets emerging around the high-symmetry paths connecting the Γ point and the central regions of the six facets within the cubic Brillouin zone. Several valence band pockets undergo the Lifshitz transition at around ~ 21 (~ 202) meV below the VBM for FeSi (OsSi), coalescing into two discrete pockets. The second valence band emerges at around ~ 13 (~ 224) meV below the VBM for FeSi (OsSi), and it undergoes a similar Lifshitz transition at lower energy, ~ 30 (~ 330) meV below the VBM for FeSi (OsSi). These features can be easily observed from the contours presented in Figs. 9 and 10. The crystal symmetries are described by the point group T , and we find that the high-symmetry points Γ and R are described by the little point group T , while M and X are characterized by D_2 [45,46]. Since the point group is achiral and nonpolar, the high-symmetry points Γ and R can host only Weyl-type spin texture, although both Weyl- and Dresselhaus-type spin textures are allowed around M and X [47]. Our calculated spin-resolved electronic structures confirm these symmetry-deduced spin distributions.

Spin accumulation. From the symmetry analysis, the CISP tensor has only diagonal components $\chi^{xx} = \chi^{yy} = \chi^{zz}$ [12], which we confirmed via explicit calculations of REE. The $\chi(E)$ plots calculated for energies below VBM are shown in Figs. 8(a) and 8(b) for FeSi and OsSi, respectively. Like in the discussion for Te/Se, we find that FeSi has a narrower energy range with substantial spin accumulation compared to OsSi owing to lower spin-orbit splitting in FeSi. The plots of $\chi(E)$ can again be rationalized by analyzing spin- and velocity-resolved isoenergy contours. For demonstration purposes, spin (s_x) and velocity (v_x) resolved contours calculated on the 001 plane and centered at Γ are shown in Figs. 9 and 10 for FeSi and OsSi, respectively. For both silicides, the peaks

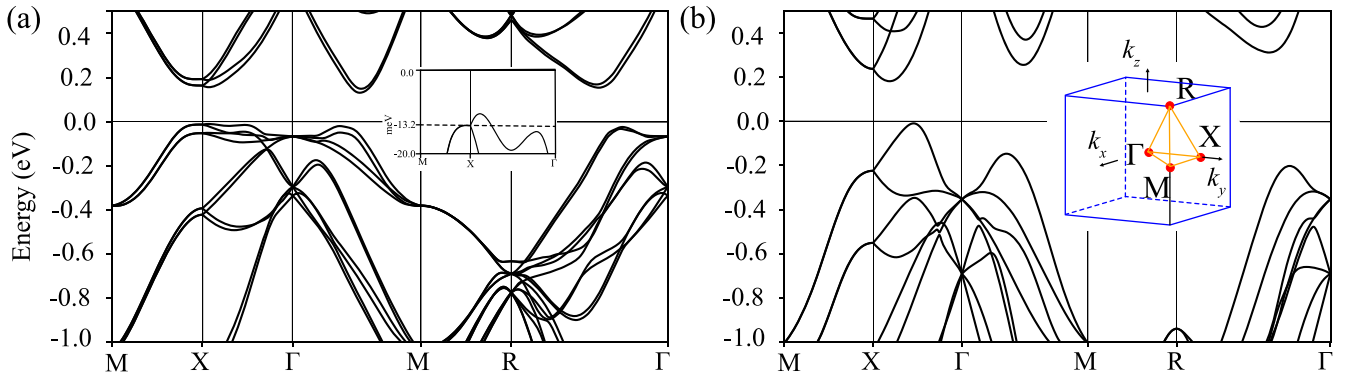


FIG. 7. (a) and (b) Relativistic electronic structures of FeSi and OsSi, respectively. The inset in (a) shows a zoomed-in view of the top and second bands of FeSi. The reference for high-symmetry lines for both (a) and (b) is shown in the inset in (b). Both materials are semiconductors, with indirect band gaps of 128 meV (FeSi) and 191 meV (OsSi). The Fermi level is set at the VBM.

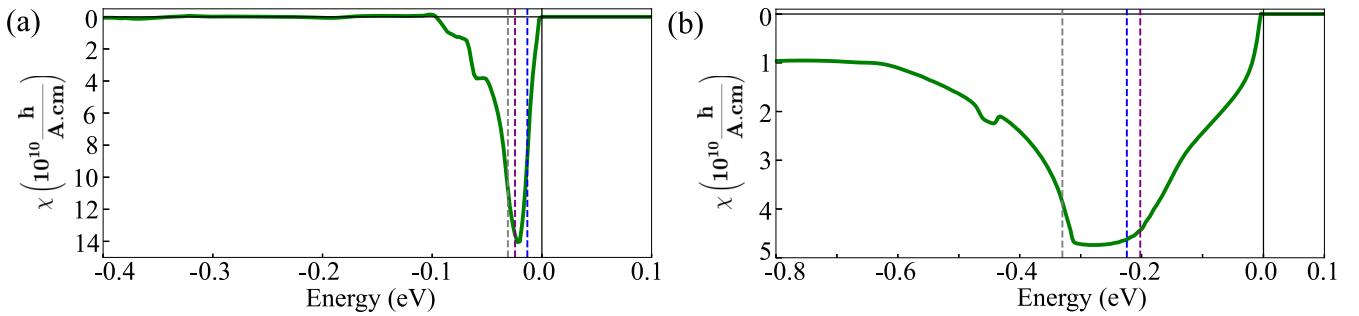


FIG. 8. (a) and (b) Current-induced spin accumulation calculated for RL-FeSi and RL-OsSi, respectively. Dashed purple line at ~ -21 (~ -202) meV for FeSi (OsSi) and gray line at ~ -31 (~ -330) meV for FeSi (OsSi) correspond to the Lifshitz transition energies of the two topmost valence bands. Blue lines indicate the edge of the second valence band at ~ -13.3 (~ -224) meV for FeSi (OsSi). Despite much stronger SOC in OsSi compared to FeSi, the spin accumulation is overall much lower.

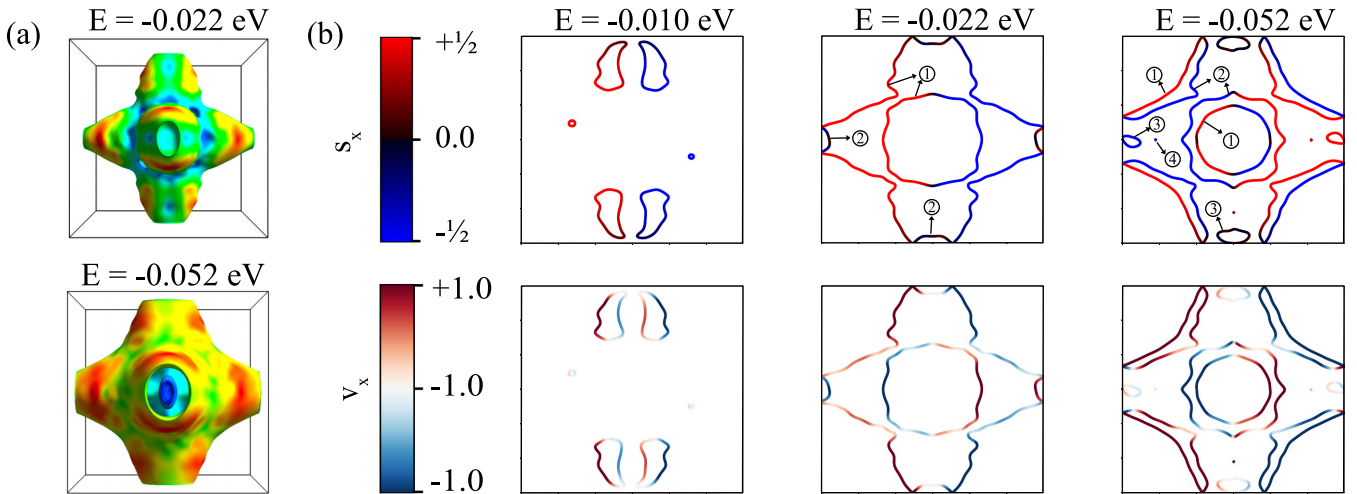


FIG. 9. (a) Isoenergy surfaces calculated for RL-FeSi at two different values of energy. The top panel shows the isoenergy surface around the energy level where the REE magnitude reaches its maximum, while the bottom panel displays a constant energy surface that corresponds to a much lower CISP. The colors represent absolute values of the Fermi velocity, with red and blue representing higher and lower values. Constant-energy surfaces were visualized using FERMISURFER [59]. (b) Top: Spin-resolved isoenergy contours sliced along the (001) plane and centered at Γ calculated for the indicated values of energies. The contour colors represent the S_x component of the spin texture scaled to $\pm\hbar/2$. Bottom: The same as above, but the color now represents the x projection of the Fermi velocity. Velocity plots are normalized to ± 1.0 corresponding to maximum/minimum values of $\pm 1.44 \frac{\text{eV bohr}}{\hbar}$. There are one, two, and four bands corresponding to the isocontours at -0.010 , -0.022 , and -0.052 eV, respectively. Band numbers are indicated if there is more than one band for a given isoenergy. Band number 1 represents the topmost band, and higher numbers denote valence bands lying deeper in energy. If the band number is not indicated, it is the topmost valence band.

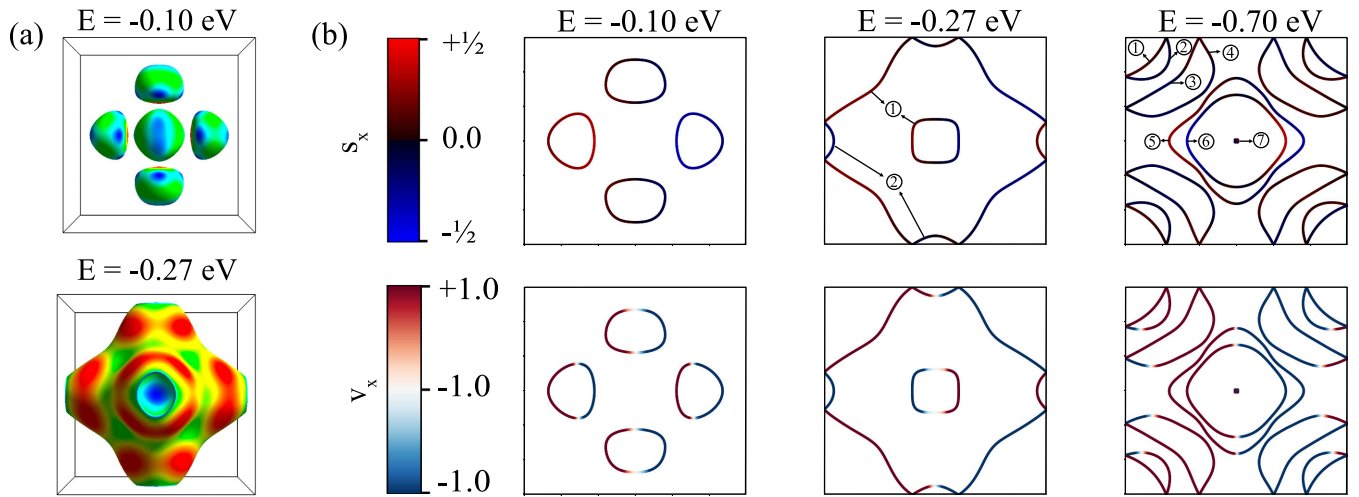


FIG. 10. Same as Fig. 9, but calculated for OsSi. Velocity plots are normalized to ± 1.0 , corresponding to maximum/minimum values of $\pm 3.62 \frac{\text{eV bohr}}{\hbar}$. There are one, two, and seven bands corresponding to the selected energies of -0.10 , -0.27 , and -0.70 eV, respectively.

in the induced spin density can be understood by examining the characteristics of the two topmost valence bands. In particular, they appear close to the Lifshitz transition energy of the valence bands. Above these transition energies, the densities diminish, although this decrease is more gradual in the case of OsSi. The compensation of spin density arising from the second valence band becomes significant only for energies below the Lifshitz transition energy of the bands since the spin density above this energy is almost negligible, which is evident from Figs. 9 and 10. A similar nature of the compensation effect among subsequent bands occurs for lower energies, as demonstrated in Fig. 9(b) [Fig. 10(b)] for an isoenergy value of ~ 52 (~ 700) meV below the VBM for FeSi (OsSi). We highlight that spin textures alone are insufficient to provide a comprehensive explanation of the current-induced spin accumulation. Instead, both spin and velocity textures have to be taken into account.

The $\chi(E)$ peak of OsSi is smaller than that of FeSi owing to the much larger charge current term in OsSi, i.e., $\sum (v_x)^2$ in the denominator of Eq. (2). In fact, the charge current is larger for OsSi not only at the energy corresponding to the peak but for all energy values considered in Fig. 8.

V. METAL DISILICIDES

Geometry and electronic structures. We now consider another pair of structurally identical materials, NbSi₂ and TaSi₂, whose right- and left-handed crystals are described by space groups $P6_222$ (180) and $P6_422$ (181), respectively. The structures, shown in Fig. 11, possess six twofold (C_2) rotational symmetries with axes within the a - b plane. Two enantiomers of the crystals can be distinguished by the opposite helicities of the pairs of X -Si- M ($X = \text{Ta/Nb}$) chains that run along the c axis, as illustrated in Fig. 11(b). The band structures calculated for TaSi₂ and NbSi₂ are displayed in Figs. 12(a) and 12(b), respectively, and they show good agreement with previous studies [11,60–62]. The Fermi surfaces, shown in Figs. 13(a)–13(d) and 14(a)–14(d), respectively, consists of two pairs of spin-split Fermi sheets. We note that the splitting energies in TaSi₂ are more than two times larger than in

NbSi₂, in agreement with the previous calculations and the measurements of the de Haas–van Alphen effect [61]. This result is not surprising, as the primary contributors to SOC in these materials are Ta 5*d* and Nb 4*d* electrons. We can also observe that the band splitting at E_F is largest close to the high-symmetry points M and K , indicating that the influence of SOC on the bands varies significantly across the BZ.

Spin textures. The spin textures corresponding to the aforementioned Fermi sheets are visualized in Figs. 13(e)–13(h) and 14(e)–14(h) for TaSi₂ and NbSi₂, respectively. For convenience, we projected them onto the planes (side rectangular faces of the BZ) centered at K and M . To understand the spin patterns, we performed group theory analysis of the high-symmetry points using the BCS server. We found that Γ , A , H , and K are described by either D_6 or D_3 point group symmetry, which allows for only Weyl-type spin texture [47]. Two other points, M and L , are described by the little point group D_2 ; thus, they can host a combination of Weyl and Dresselhaus SOCs [47]. These findings agree with the first-principles results; the spin patterns around the K point are radial, alternating between outward and inward orientation for two subsequent bands, 102 and 103. Also the spin texture of the band centered at the M point is predominantly radial

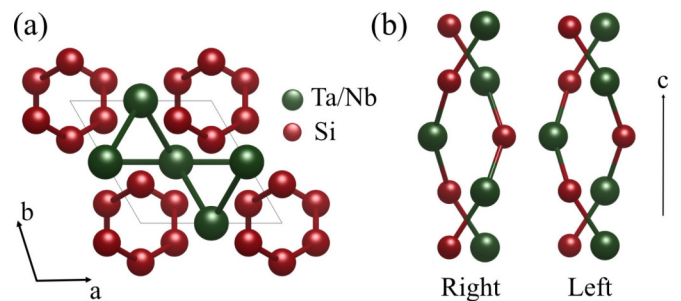


FIG. 11. (a) Top view of TaSi₂ and NbSi₂ crystal structures. (b) Side view of their right- and left-handed enantiomers. The chirality is determined by the opposite helicity of the pair of spiral chains running along the c axis (SGs 180 and 181).

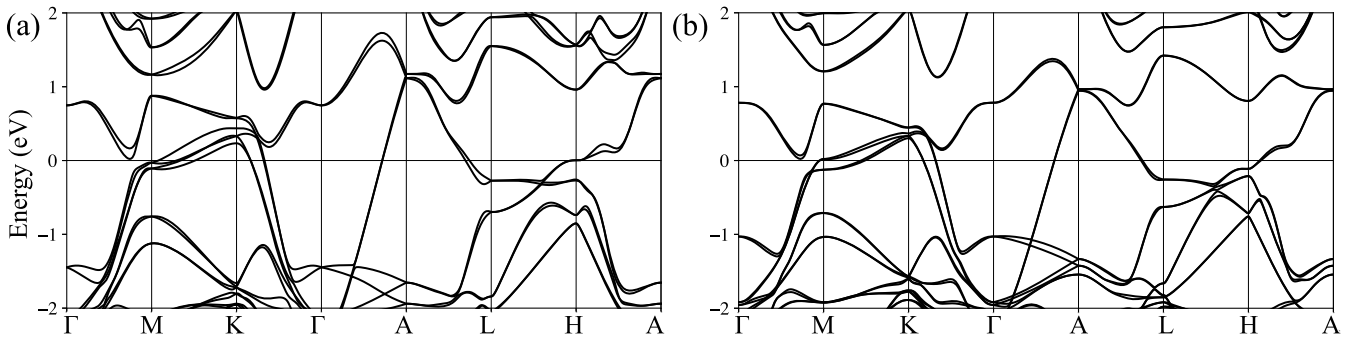


FIG. 12. (a) Band structure of TaSi₂ along the high-symmetry lines sketched in Fig. 1 (c). (b) The same as (a), but for NbSi₂.

[Figs. 13(e) and 13(f) and 14(e) and 14(f)], with tangential components visible only close to the corners of the plot for TaSi₂ [Figs. 13(g) and 13(h)] and around the *M* point for NbSi₂ [Figs. 14(g) and 14(h)].

Spin accumulation. Experimental studies of chirality-dependent spin transport in metal disilicides revealed spin signals due to the electric current flowing along the chiral axis [15]. In our recent study, we suggested that such results could be attributed to the collinear REE occurring in TaSi₂ due to the presence of dominant Weyl-type SOF [11]. However, similar to the elemental semiconductors, the REE tensor has three (two independent) components, $\chi^{xx} = \chi^{yy}$ and χ^{zz} [12], and the former were not investigated experimentally.

The magnitudes of the different components of the χ tensor calculated as a function of the chemical potential are plotted

in Figs. 15(a) and 15(b) for TaSi₂ and NbSi₂, respectively. Surprisingly, in TaSi₂, we observe an even higher value of χ^{xx} than χ^{zz} at the Fermi level, and in NbSi₂ these two components are nearly equal. Despite their complicated electronic structures, the spin accumulation results can be rationalized to some extent based on the spin textures shown in Figs. 13 and 14. Like in Te, two inner pockets display radial spin texture, but with spins polarized more uniformly than in Te. The outer two surfaces are extended isoenergy surfaces with spins mostly polarized along the k_z direction for large parts of the surface on k_x - k_y planes, while the spins on the six faces of the BZ have signatures of Dresselhaus-type textures. Moreover, the band velocities are high in all directions, which may explain why the values of REE at E_F are nearly two orders of magnitude lower than in Te.

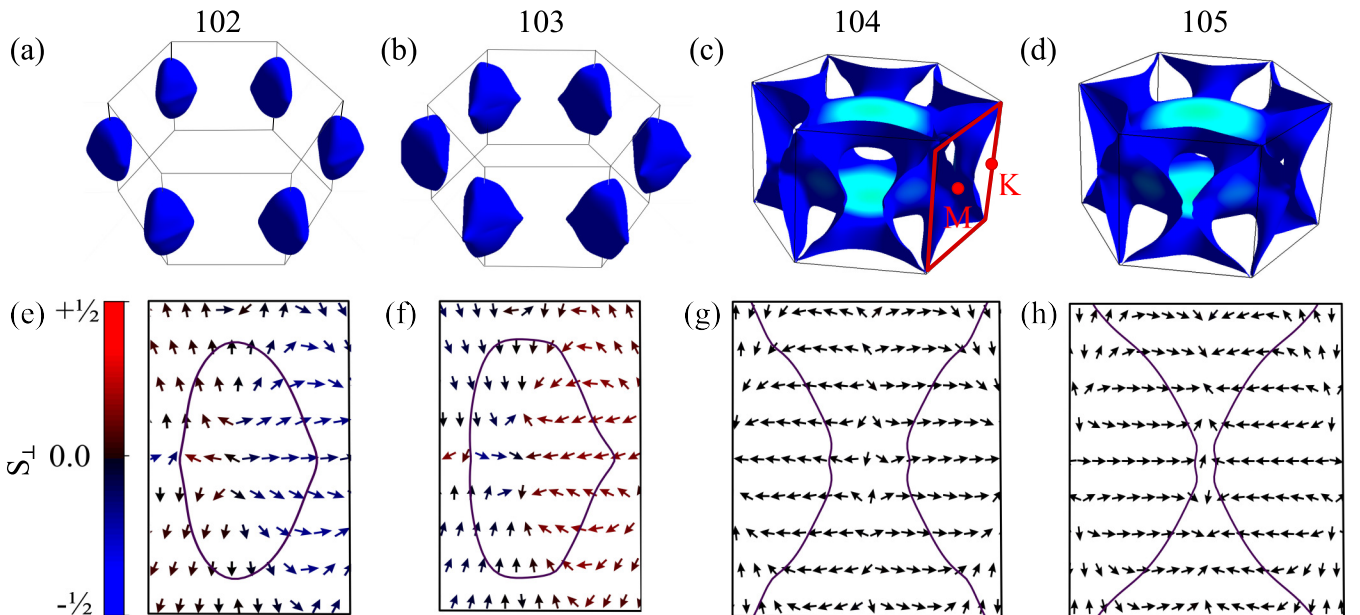
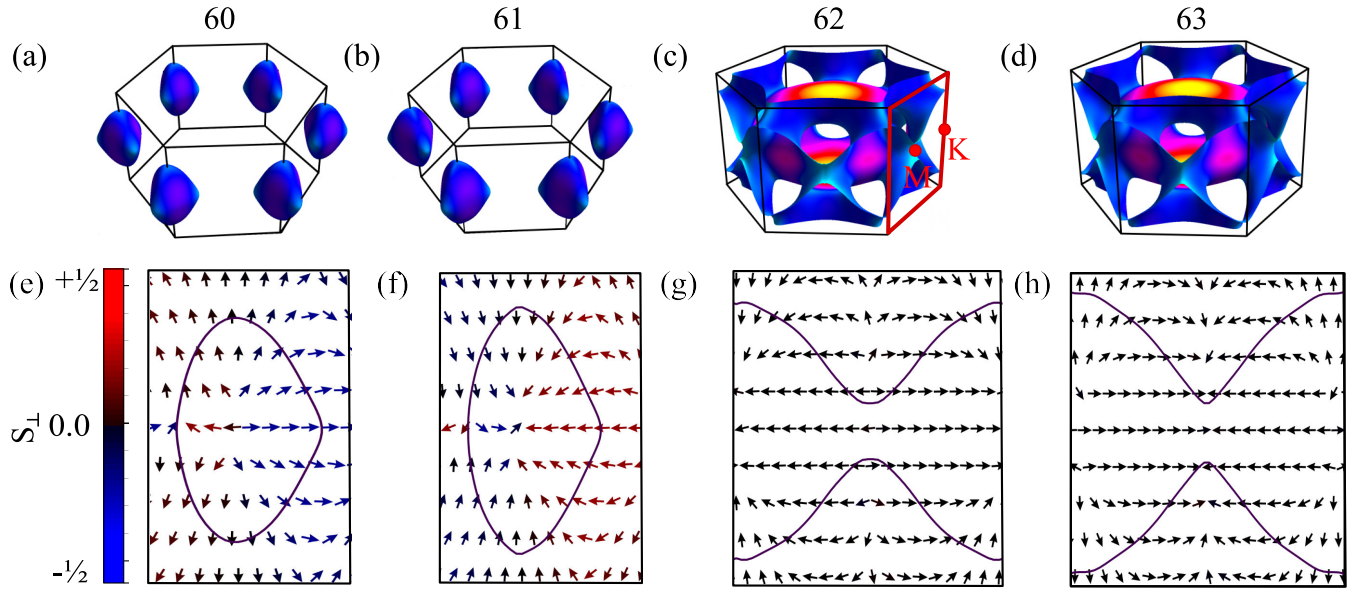


FIG. 13. (a)–(d) Fermi surfaces of TaSi₂ calculated at the Fermi level. Bands numbered 102 and 103 are ellipsoid, centered at the *K* points, while bands 104 and 105 are open surfaces whose projections at each of the rectangular faces of the BZ are hyperbolic-shaped contours around the *M* points. The colors are used to distinguish the inner and outer parts of the surfaces. Axis directions of the BZ are in accordance with Fig. 1(c). (e) Spin texture of band 102 projected onto the side face of the BZ and centered at the *K* point. The contour corresponds to $E = E_F$. (f) The same, plotted for band 103. (g) The same as (e) and (f) calculated for band 104 and centered around the *M* point. (h) The same as (g) plotted for band 105. The spin textures around the *K* points follow a purely Weyl-type SOC, and those around the *M* points reveal a Weyl-Dresselhaus SOF. The arrow colors indicate spin components normal to the planes. The k_z axis is along the vertical direction for all spin texture plots.

FIG. 14. The same as Fig. 13, but calculated for NbSi₂.

The two disilicides have comparable REEs because their Fermi surfaces and the corresponding spin textures which give rise to the spin accumulation are overall quite similar. Differences in the magnitudes of χ can be attributed to the fact that the spin splitting of the bands is larger in TaSi₂ than in NbSi₂, which affects the nature of spin accumulation compensation, as discussed in the previous section. Differences in band splitting can be noticed in Figs. 12(a) and 12(b), close to E_F and along the crystallographic directions ΓM , AH , AL , and MK that determine the magnitudes of the χ^{xx} and χ^{yy} tensor components. The weaker SOC in NbSi₂ gives rise to nearly degenerate bands, and their contributions to the effective spin accumulation nullify each other, similar to what happens in the case of Se. Our results for metal disilicides are thus consistent with the conclusions drawn in the previous sections.

VI. CONCLUSIONS

In conclusion, we studied the chirality-dependent collinear REE in a few representative materials, focusing on the role of SOC. We found that unconventional spin accumulation is favorable in crystals that host one particular type of spin texture, radial for chiral materials, which gives rise to parallel spin-momentum locking. We observed that the magnitude of the induced spin density is sensitive to both the spin polarization of bands in the momentum space and band velocities. For example, the bands of Te are highly spin polarized along the screw axis, which implies the highest spin accumulation along this direction, whereas the spin texture is more isotropic in Se, leading to almost equal magnitudes of χ along different axes. The values, as a function of the chemical potential, are additionally modulated by the band velocities.

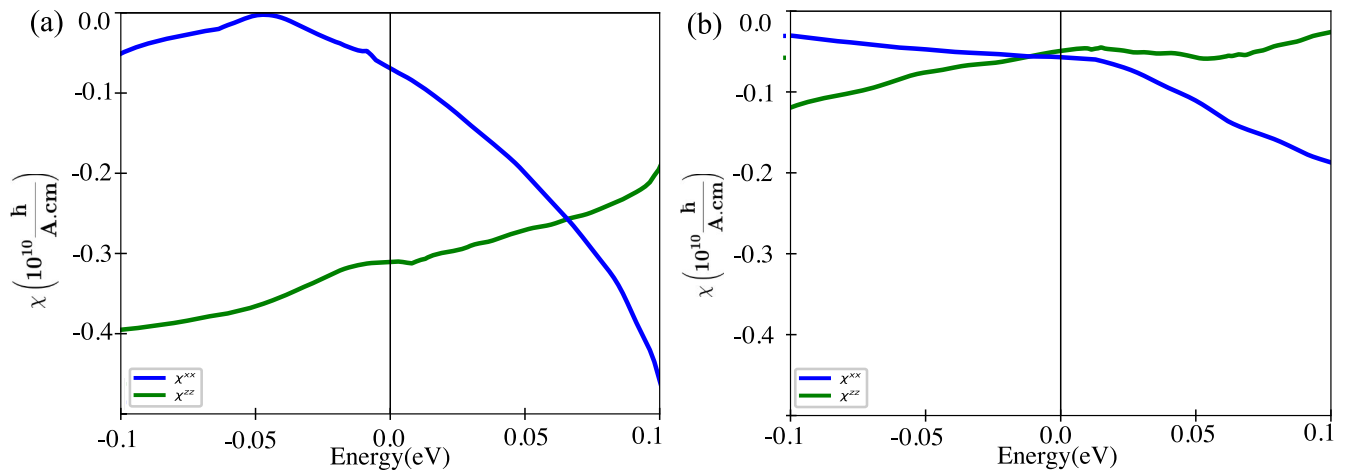


FIG. 15. (a) CISP tensor of left-handed TaSi₂ calculated as a function of the chemical potential. Different tensor components are distinguished by colors. (b) Same as (a) calculated for the left-handed NbSi₂. The components χ^{yy} are omitted, as they are equal to χ^{xx} .

The effect of the strength of SOC is more subtle to analyze [63]. On the one hand, the spin-orbit interaction lifts both energy and spin degeneracy of noncentrosymmetric crystal structures, and it is a necessary condition for the emergence of the REE [12]. On the other hand, the high SOC does not *per se* lead to large magnitudes of the REE. Note that two chiral disilicides with different strengths of SOC show similar χ around E_F , while OsSi with larger SOC yields smaller spin accumulation compared to FeSi. Our results reveal that stronger SOI provides larger spin splitting of the bands and often prevents compensating the spin accumulation that originates from oppositely spin-polarized bands. It can therefore indirectly increase the REE, but only in the energy regions where the band splitting is significant.

Our research on the collinear REE in chiral materials has practical applications in the design of spintronic devices that use spin-to-charge conversion in unconventional configurations. Additionally, it provides a valuable reference for computational studies searching for materials with the high conversion efficiency. Even though it is difficult to predict the magnitude of the REE without explicitly calculating the

electronic structure, it will guide high-throughput simulations and facilitate their analysis. Finally, we clarified the role of SOC, which is believed to be crucial for observing the REE in solid-state materials, and we highlighted the significance of band velocities that may contribute to the effect. This could be relevant for investigations of CISS, which can manifest even in systems with weak SOC. Last, we emphasized the potentially crucial role of orbital effects, which must also be incorporated in the future for a comprehensive analysis of CISS [64–66].

ACKNOWLEDGMENTS

J.S. acknowledges the Rosalind Franklin Fellowship from the University of Groningen. The calculations were carried out on the Dutch national e-infrastructure with the support of the SURF Cooperative (EINF-2070), on the Peregrine high-performance computing cluster of the University of Groningen, and at the Texas Advanced Computing Center at the University of Texas at Austin.

-
- [1] L. D. Barron, True and false chirality and absolute asymmetric synthesis, *J. Am. Chem. Soc.* **108**, 5539 (1986).
- [2] C. Kallin and J. Berlinsky, Chiral superconductors, *Rep. Prog. Phys.* **79**, 054502 (2016).
- [3] G. Chang, B. J. Wieder, F. Schindler, D. S. Sanchez, I. Belopolski, S.-M. Huang, B. Singh, D. Wu, T.-R. Chang, T. Neupert, S.-Y. Xu, H. Lin, and M. Z. Hasan, Topological quantum properties of chiral crystals, *Nat. Mater.* **17**, 978 (2018).
- [4] Y. Tokunaga, X. Yu, J. White, H. M. Rønnow, D. Morikawa, Y. Taguchi, and Y. Tokura, A new class of chiral materials hosting magnetic skyrmions beyond room temperature, *Nat. Commun.* **6**, 7638 (2015).
- [5] A. Chacon, L. Heinen, M. Halder, A. Bauer, W. Simeth, S. Mühlbauer, H. Berger, M. Garst, A. Rosch, and C. Pfleiderer, Observation of two independent skyrmion phases in a chiral magnetic material, *Nat. Phys.* **14**, 936 (2018).
- [6] K. Ray, S. Ananthavel, D. Waldeck, and R. Naaman, Asymmetric scattering of polarized electrons by organized organic films of chiral molecules, *Science* **283**, 814 (1999).
- [7] R. Naaman and D. H. Waldeck, Spintronics and chirality: Spin selectivity in electron transport through chiral molecules, *Annu. Rev. Phys. Chem.* **66**, 263 (2015).
- [8] S.-H. Yang, R. Naaman, Y. Paltiel, and S. S. Parkin, Chiral spintronics, *Nat. Rev. Phys.* **3**, 328 (2021).
- [9] T. Furukawa, Y. Shimokawa, K. Kobayashi, and T. Itou, Observation of current-induced bulk magnetization in elemental tellurium, *Nat. Commun.* **8**, 954 (2017).
- [10] F. Calavalle, M. Suárez-Rodríguez, B. Martín-García, A. Johansson, D. C. Vaz, H. Yang, I. V. Maznichenko, S. Ostanin, A. Mateo-Alonso, A. Chuvilin *et al.*, Gate-tunable and chirality-dependent charge-to-spin conversion in tellurium nanowires, *Nat. Mater.* **21**, 526 (2022).
- [11] A. Roy, F. T. Cerasoli, A. Jayaraj, K. Tenzin, M. Buongiorno Nardelli, and J. Sławińska, Long-range current-induced spin accumulation in chiral crystals, *npj Comput. Mater.* **8**, 243 (2022).
- [12] K. Tenzin, A. Roy, H. Jafari, B. Banas, F. T. Cerasoli, M. Date, A. Jayaraj, M. Buongiorno Nardelli, and J. Sławińska, Analogs of Rashba-Edelstein effect from density functional theory, *Phys. Rev. B* **107**, 165140 (2023).
- [13] A. Inui, R. Aoki, Y. Nishiue, K. Shiota, Y. Kousaka, H. Shishido, D. Hirobe, M. Suda, J.-i. Ohe, J.-i. Kishine, H. M. Yamamoto, and Y. Togawa, Chirality-induced spin-polarized state of a chiral crystal CrNb₃S₆, *Phys. Rev. Lett.* **124**, 166602 (2020).
- [14] H. Shishido, R. Sakai, Y. Hosaka, and Y. Togawa, Detection of chirality-induced spin polarization over millimeters in polycrystalline bulk samples of chiral disilicides NbSi₂ and TaSi₂, *Appl. Phys. Lett.* **119**, 182403 (2021).
- [15] K. Shiota, A. Inui, Y. Hosaka, R. Amano, Y. Ōnuki, M. Hedo, T. Nakama, D. Hirobe, J.-i. Ohe, J.-i. Kishine, H. M. Yamamoto, H. Shishido, and Y. Togawa, Chirality-induced spin polarization over macroscopic distances in chiral disilicide crystals, *Phys. Rev. Lett.* **127**, 126602 (2021).
- [16] P. Giannozzi *et al.*, QUANTUM ESPRESSO: A modular and open-source software project for quantum simulations of materials, *J. Phys.: Condens. Matter* **21**, 395502 (2009).
- [17] P. Giannozzi *et al.*, Advanced capabilities for materials modelling with QUANTUM ESPRESSO, *J. Phys.: Condens. Matter* **29**, 465901 (2017).
- [18] A. D. Corso, Pseudopotentials periodic table: From H to Pu, *Comput. Mater. Sci.* **95**, 337 (2014).
- [19] J. P. Perdew, K. Burke, and M. Ernzerhof, Generalized gradient approximation made simple, *Phys. Rev. Lett.* **77**, 3865 (1996).
- [20] J. P. Perdew, A. Ruzsinszky, G. I. Csonka, O. A. Vydrov, G. E. Scuseria, L. A. Constantin, X. Zhou, and K. Burke, Restoring the density-gradient expansion for exchange in solids and surfaces, *Phys. Rev. Lett.* **100**, 136406 (2008).
- [21] H. Sakamoto, A. Fujii, K. Tanaka, and H. Inui, Enantiomorph identification of transition-metal disilicides with the C40 structure (the space group of $P6_22$ and $P6_422$)

- by new convergent-beam electron diffraction method, *Acta Mater.* **53**, 41 (2005).
- [22] L. A. Agapito, S. Curtarolo, and M. Buongiorno Nardelli, Reformulation of DFT $+U$ as a pseudohybrid Hubbard density functional for accelerated materials discovery, *Phys. Rev. X* **5**, 011006 (2015).
- [23] M. Buongiorno Nardelli, F. T. Cerasoli, M. Costa, S. Curtarolo, R. D. Gennaro, M. Fornari, L. Liyanage, A. R. Supka, and H. Wang, PAOFLOW: A utility to construct and operate on ab initio Hamiltonians from the projections of electronic wavefunctions on atomic orbital bases, including characterization of topological materials, *Comput. Mater. Sci.* **143**, 462 (2018).
- [24] F. T. Cerasoli, A. R. Supka, A. Jayaraj, M. Costa, I. Siloi, J. Sławińska, S. Curtarolo, M. Fornari, D. Ceresoli, and M. Buongiorno Nardelli, Advanced modeling of materials with PAOFLOW 2.0: New features and software design, *Comput. Mater. Sci.* **200**, 110828 (2021).
- [25] L. A. Agapito, S. Ismail-Beigi, S. Curtarolo, M. Fornari, and M. B. Nardelli, Accurate tight-binding Hamiltonian matrices from *ab initio* calculations: Minimal basis sets, *Phys. Rev. B* **93**, 035104 (2016).
- [26] L. A. Agapito, M. Fornari, D. Ceresoli, A. Ferretti, S. Curtarolo, and M. B. Nardelli, Accurate tight-binding Hamiltonians for two-dimensional and layered materials, *Phys. Rev. B* **93**, 125137 (2016).
- [27] J. R. Yates, X. Wang, D. Vanderbilt, and I. Souza, Spectral and Fermi surface properties from Wannier interpolation, *Phys. Rev. B* **75**, 195121 (2007).
- [28] N. W. Ashcroft and N. D. Mermin, The semiclassical theory of conduction in metals, in *Solid State Physics* (Holt, Rinehart and Winston, New York, 1976), Chap. 13, pp. 243–262.
- [29] P. L. Taylor and O. Heinonen, The semiclassical theory of conductivity in metals, in *A Quantum Approach to Condensed Matter Physics* (Cambridge University Press, Cambridge, 2002), Chap. 8, pp. 285–339.
- [30] J. M. Ziman, Transport properties, in *Principles of Theory of Solids* (Cambridge University Press, Cambridge, 1972), Chap. 7, pp. 211–254.
- [31] A. Roy, M. H. D. Guimarães, and J. Sławińska, Unconventional spin Hall effects in nonmagnetic solids, *Phys. Rev. Mater.* **6**, 045004 (2022).
- [32] M. Hirayama, R. Okugawa, S. Ishibashi, S. Murakami, and T. Miyake, Weyl node and spin texture in trigonal tellurium and selenium, *Phys. Rev. Lett.* **114**, 206401 (2015).
- [33] G. Gatti *et al.*, Radial spin texture of the Weyl fermions in chiral tellurium, *Phys. Rev. Lett.* **125**, 216402 (2020).
- [34] M. Sakano *et al.*, Radial spin texture in elemental tellurium with chiral crystal structure, *Phys. Rev. Lett.* **124**, 136404 (2020).
- [35] V. Anzin, M. Eremets, Y. V. Kossichkin, A. Nadezhdinskii, and A. Shirokov, Measurement of the energy gap in tellurium under pressure, *Phys. Status Solidi A* **42**, 385 (1977).
- [36] E. Streltsov, S. Poznyak, and N. Osipovich, Photoinduced and dark underpotential deposition of lead on selenium, *J. Electroanal. Chem.* **518**, 103 (2002).
- [37] A. Bhatnagar, K. V. Reddy, and V. Srivastava, Optical energy gap of amorphous selenium: Effect of annealing, *J. Phys. D* **18**, L149 (1985).
- [38] S. Tutihasi and I. Chen, Optical properties and band structure of trigonal selenium, *Phys. Rev.* **158**, 623 (1967).
- [39] N. Zhang, G. Zhao, L. Li, P. Wang, L. Xie, B. Cheng, H. Li, Z. Lin, C. Xi, J. Ke, M. Yang, J. He, Z. Sun, Z. Wang, Z. Zhang, and C. Zeng, Magnetotransport signatures of Weyl physics and discrete scale invariance in the elemental semiconductor tellurium, *Proc. Natl. Acad. Sci. USA* **117**, 11337 (2020).
- [40] T. Ideue, M. Hirayama, H. Taiko, T. Takahashi, M. Murase, T. Miyake, S. Murakami, T. Sasagawa, and Y. Iwasa, Pressure-induced topological phase transition in noncentrosymmetric elemental tellurium, *Proc. Natl. Acad. Sci. USA* **116**, 25530 (2019).
- [41] A. Stoliaroff, C. Latouche, and S. Jobic, Impact of point defects on the electrical properties of selenium: A density functional theory investigation with discussion of the entropic term, *Phys. Rev. B* **103**, 094111 (2021).
- [42] W. F. Waller, *Electronics Design Materials* (Springer, Berlin, 1971).
- [43] U. Fano and W. Martin, Z-dependence of spin-orbit coupling, in *Topics in Modern Physics, A Tribute to E. U. Condon*, edited by W. E. Brittin and H. Odabasi (Colorado Associated University Press, 1971), pp. 147–152.
- [44] W. C. Martin, Table of spin-orbit energies for p -electrons in neutral atomic (core) np configurations, *J. Res. Natl. Bur. Stand., Sect. A* **75A**, 109 (1971).
- [45] M. I. Aroyo, J. M. Perez-Mato, C. Capillas, E. Kroumova, S. Ivantchev, G. Madariaga, A. Kirov, and H. Wondratschek, Bilbao Crystallographic Server: I. Databases and crystallographic computing programs, *Z. Kristallogr. - Cryst. Mater.* **221**, 15 (2006).
- [46] M. I. Aroyo, A. Kirov, C. Capillas, J. M. Perez-Mato, and H. Wondratschek, Bilbao Crystallographic Server. II. Representations of crystallographic point groups and space groups, *Acta Crystallogr., Sect. A* **62**, 115 (2006).
- [47] C. Mera Acosta, L. Yuan, G. M. Dalpian, and A. Zunger, Different shapes of spin textures as a journey through the Brillouin zone, *Phys. Rev. B* **104**, 104408 (2021).
- [48] D. G. Martinez, A. Crepaldi, and O. V. Yazyev, Diversity of radial spin textures in chiral materials, *Phys. Rev. B* **108**, L201114 (2023).
- [49] L. L. Tao and E. Y. Tsymbal, Persistent spin texture enforced by symmetry, *Nat. Commun.* **9**, 2763 (2018).
- [50] J. Sławińska, F. T. Cerasoli, P. Gopal, M. Costa, S. Curtarolo, and M. Buongiorno Nardelli, Ultrathin SnTe films as a route towards all-in-one spintronics devices, *2D Mater.* **7**, 025026 (2020).
- [51] A. Johansson, J. Henk, and I. Mertig, Theoretical aspects of the Edelstein effect for anisotropic two-dimensional electron gas and topological insulators, *Phys. Rev. B* **93**, 195440 (2016).
- [52] P. Tang, Q. Zhou, and S.-C. Zhang, Multiple types of topological fermions in transition metal silicides, *Phys. Rev. Lett.* **119**, 206402 (2017).
- [53] G. Chang, S.-Y. Xu, B. J. Wieder, D. S. Sanchez, S.-M. Huang, I. Belopolski, T.-R. Chang, S. Zhang, A. Bansil, H. Lin, and M. Z. Hasan, Unconventional chiral fermions and large topological Fermi arcs in RhSi, *Phys. Rev. Lett.* **119**, 206401 (2017).
- [54] Z. Rao, H. Li, T. Zhang, S. Tian, C. Li, B. Fu, C. Tang, L. Wang, Z. Li, W. Fan *et al.*, Observation of unconventional chiral fermions with long Fermi arcs in CoSi, *Nature (London)* **567**, 496 (2019).
- [55] D. Takane, Z. Wang, S. Souma, K. Nakayama, T. Nakamura, H. Oinuma, Y. Nakata, H. Iwasawa, C. Cacho, T. Kim, K.

- Horiba, H. Kumigashira, T. Takahashi, Y. Ando, and T. Sato, Observation of chiral fermions with a large topological charge and associated Fermi-arc surface states in CoSi, *Phys. Rev. Lett.* **122**, 076402 (2019).
- [56] G. H. Fecher, J. Kübler, and C. Felser, Chirality in the solid state: Chiral crystal structures in chiral and achiral space groups, *Materials* **15**, 5812 (2022).
- [57] D. A. Pshenay-Severin and A. T. Burkov, Electronic structure of B20 (FeSi-type) transition-metal monosilicides, *Materials* **12**, 2710 (2019).
- [58] S. Changdar, S. Aswartham, A. Bose, Y. Kushnirenko, G. Shipunov, N. C. Plumb, M. Shi, A. Narayan, B. Büchner, and S. Thirupathiah, Electronic structure studies of FeSi: A chiral topological system, *Phys. Rev. B* **101**, 235105 (2020).
- [59] M. Kawamura, FermiSurfer: Fermi-surface viewer providing multiple representation schemes, *Comput. Phys. Commun.* **239**, 197 (2019).
- [60] C. A. C. Garcia, D. M. Nenno, G. Varnavides, and P. Narang, Anisotropic phonon-mediated electronic transport in chiral Weyl semimetals, *Phys. Rev. Mater.* **5**, L091202 (2021).
- [61] Y. Ōnuki, A. Nakamura, T. Uejo, A. Teruya, M. Hedo, T. Nakama, F. Honda, and H. Harima, Chiral-structure-driven split Fermi surface properties in TaSi₂, NbSi₂, and VSi₂, *J. Phys. Soc. Jpn.* **83**, 061018 (2014).
- [62] J. Zhang, Y.-H. Chan, C.-K. Chiu, M. G. Vergniory, L. M. Schoop, and A. P. Schnyder, Topological band crossings in hexagonal materials, *Phys. Rev. Mater.* **2**, 074201 (2018).
- [63] M.-H. Liu, S.-H. Chen, C.-R. Chang *et al.*, Current-induced spin polarization in spin-orbit-coupled electron systems, *Phys. Rev. B* **78**, 165316 (2008).
- [64] Y.-G. Choi, D. Jo, K.-H. Ko, D. Go, K.-H. Kim, H. G. Park, C. Kim, B.-C. Min, G.-M. Choi, and H.-W. Lee, Observation of the orbital Hall effect in a light metal Ti, *Nature (London)* **619**, 52 (2023).
- [65] T. Yoda, T. Yokoyama, and S. Murakami, Current-induced orbital and spin magnetizations in crystals with helical structure, *Sci. Rep.* **5**, 12024 (2015).
- [66] T. Yoda, T. Yokoyama, and S. Murakami, Orbital Edelstein effect as a condensed-matter analog of solenoids, *Nano Lett.* **18**, 916 (2018).